Supplementary information for: Integrated Microcomb-Driven Vortex Electromagnetic Waves for Broadband Forward-looking Sensing

Guanqun Sun[1†], Zhekai Zheng[2†], Jiacheng Guo[2], Wenjun Qi[3], Ding Cui[2], Hao Zhang[2*], Jijun He[2*], Fangzheng Zhang[2*], Yiping Wang[1*], Shilong Pan[2*]

[1*]School of Computer and Electronic Information, Nanjing Normal University, Nanjing, 210023, China.
[2]National Key Laboratory of Microwave Photonics, Nanjing University of Aeronautics and Astronautics, Nanjing 210016, China.
[3]College of Information Science and Engineering, Hohai University, Nanjing 210024, China.

*Corresponding author(s). E-mail(s): jamzhang627@gmail.com; jijun.he@nuaa.edu.cn; zhangfangzheng@nuaa.edu.cn; ypwang@njnu.edu.cn; pans@nuaa.edu.cn;
Contributing authors: sunguanqun@nnu.edu.cn; zhengzk@nuaa.edu.cn; guojc452@nuaa.edu.cn; qiwenjun@hhu.edu.cn; cdjinge@nuaa.edu.cn;
†These authors contributed equally to this work.

Contents

Supplementary Notes:

Supplementary Figures:

Supplementary Note 1. Device Characterization

The experimental demonstration of the broadband vortex electromagnetic (EM) sensing system relies on a high-performance integrated microwave photonic architecture. This section details the characterization of the core photonic engines (packaged for experimental prototyping) corroborating the system parameters reported in the main text.

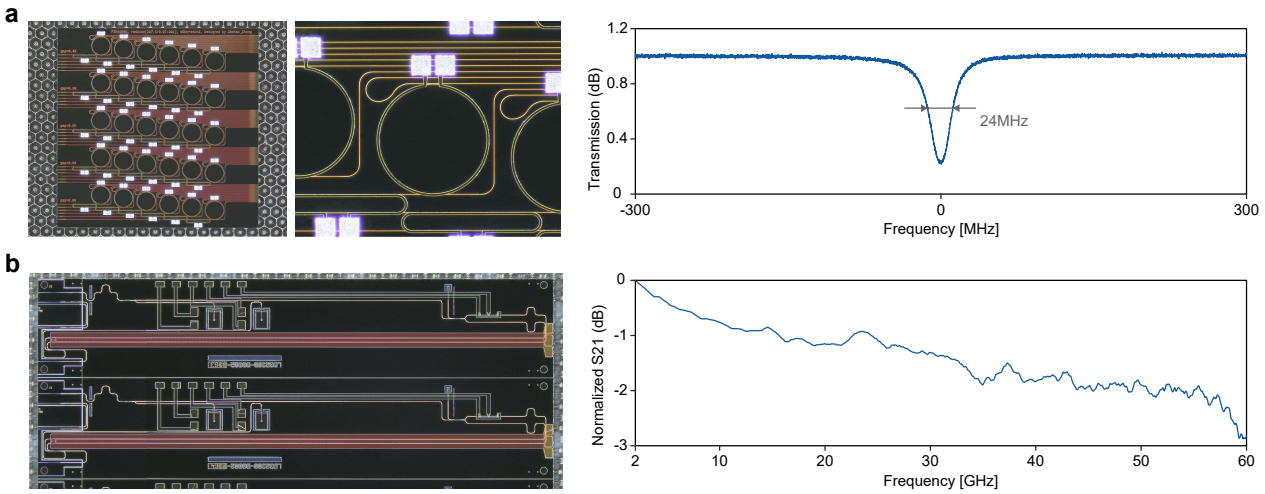

Figure S1. **Device-level characterization of the photonic source and modulator. a.** Photograph and representative transmission response of the Si_3N_4 MRR used for Kerr-comb generation. **b.** Photograph and electro-optic response of the thin-film lithium-niobate MZM.

Fig. S1 summarizes the performance of the chip-scale components used in the broadband vortex EM sensing system. The Kerr-comb used in the experiment are generated by a high-Q Si_3N_4 micro-ring resonator (MRR) fabricated by the Qaleido Photonics. The device features a radius of $238\mu m$ and a waveguide cross-section of $0.8 \times 1.77\mu m$, designed to yield a Free Spectral Range (FSR) of approximately 100 GHz. Its optical micrograph and transmission characteristics are shown in Figure. S1a, where the resonance exhibits a full width at half maximum (FWHM) of 24 MHz, corresponding to a quality factor of 8×10^6. This ultra-high Q factor is the physical prerequisite for accessing the dissipative Kerr soliton (DKS) regime.

To support the generation of multi-channel broadband frequency-swept signals, we employ a thin-film lithium-niobate Mach–Zehnder modulator (MZM) fabricated by Liobate Co., Ltd.. The device's electro-optic response, shown in Figure. S1b, demonstrates a 3-dB bandwidth exceeding 50 GHz. This wide modulation bandwidth, significantly surpassing the operation range of the K-band system, ensures the modulation efficiency for the generated frequency-swept signals.

Supplementary Note 2. Vortex EM Field Measurement Environment and System

This note describes the measurement environment and data-acquisition procedure used for the field characterization reported in the main text. Radiation-field measurements were carried out in a microwave anechoic chamber using an automated scanning system. The experimental testbed comprises a central workstation that synchronizes a vector network analyzer (VNA) with a three-dimensional electronic scanning frame. The transmission link incorporates the proposed microcomb-driven generation system feeding a 16-element K-band Uniform Circular Array (UCA), while the receiving end employs a standard open-ended rectangular waveguide probe mounted on the scanner to collect the electromagnetic field data. The central workstation manages the precise positioning of the probe and triggers the VNA for data acquisition at each spatial sampling point, enabling precise mapping of the radiation characteristics.

Prior to the vortex beam measurement, channel-to-channel amplitude imbalance and phase error introduced by the optical paths, fibres and electrical cables were compensated through the programmable optical signal processor. During the measurement, the receiving probe was positioned at a distance of z = 3 m from the transmitting UCA plane to capture the radiation fields. The probe performed a raster scan over a 2D transverse plane covering an area of 1000 mm × 1000 mm with a step size of 10 mm in both horizontal and vertical directions. At each spatial grid point, the VNA performed a stepped-frequency sweep from 18 to 26 GHz with 4001 frequency sampling points. The collected complex S-parameter data (S21) formed the basis for the field analysis and Orbital Angular Momentum (OAM) spectral decomposition presented in the main text.

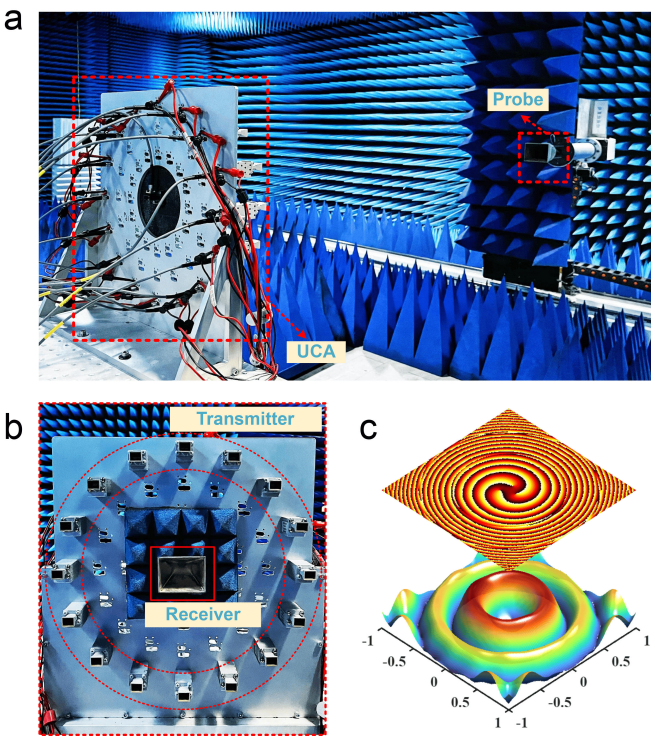

Figure S2. Experimental testbed for vortex EM wave characterization. a. Photograph of the 16-element UCA transmitter. **b.** Field measurement environment inside the microwave anechoic chamber. **c.** Representative measured radiation intensity and phase distributions for an OAM mode l=3 measured at 18 GHz.

Supplementary Note 3: Evaluation Metrics for Vortex Electromagnetic Fields

This note summarizes the definitions of the two metrics used in the main text to quantify the quality of the generated vortex electromagnetic (EM) waves: the Fundamental-mode Energy Ratio (FER) and the Degree of Intensity Deviation (DID) [1]. It also provides extended FER measurements covering a wider range of frequencies and OAM modes to corroborate the system's robustness.

The FER evaluates the spectral purity of the generated vortex beam. It is defined as the ratio of the energy contained in the target OAM mode l_{target} to the total energy of all measurable OAM modes in the spectrum. Based on the azimuth Fourier coefficients C_n derived from the measured field at a fixed elevation angle, the FER is calculated as:

$$\text{FER} = \frac{|C_{l_{target}}|^2}{\sum_{n=-\infty}^{+\infty} |C_n|^2} \tag{1}$$

A higher FER value (closer to 1) indicates higher spectral purity and less energy leakage into adjacent spurious modes (mode aliasing).

The DID metric quantifies the structural integrity of the amplitude profile. For an ideal pure-state vortex EM wave, the radiation intensity is invariant with respect to the azimuth angle, meaning that the radiation intensity at the same elevation position is identical. However, practical amplitude imbalance or phase errors often break this symmetry. The DID is therefore defined as:

$$\begin{aligned} \text{DID} &= \frac{1}{MG^2} \sum_{m=1}^{M} (x_m - \bar{x})^2 \\ x_m &= \frac{\hat{x}_m \cdot r}{N} \\ G &= \bar{x} / J_l(ka \sin\theta) \end{aligned} \tag{2}$$

Where M is the number of sampling points along the azimuthal circle. $\hat{x}_m$ is the measured intensity at the sampling point m. $\bar{x}$ is the average intensity calculated over the sampling circle. A lower DID value (closer to 0) indicates that the generated beam possesses better rotational symmetry and structural quality.

Figure S3 extends the FER characterization beyond the representative l=3 case shown in the main text to validate the capabilities and robustness of the proposed architecture. The DKS microcomb-driven system

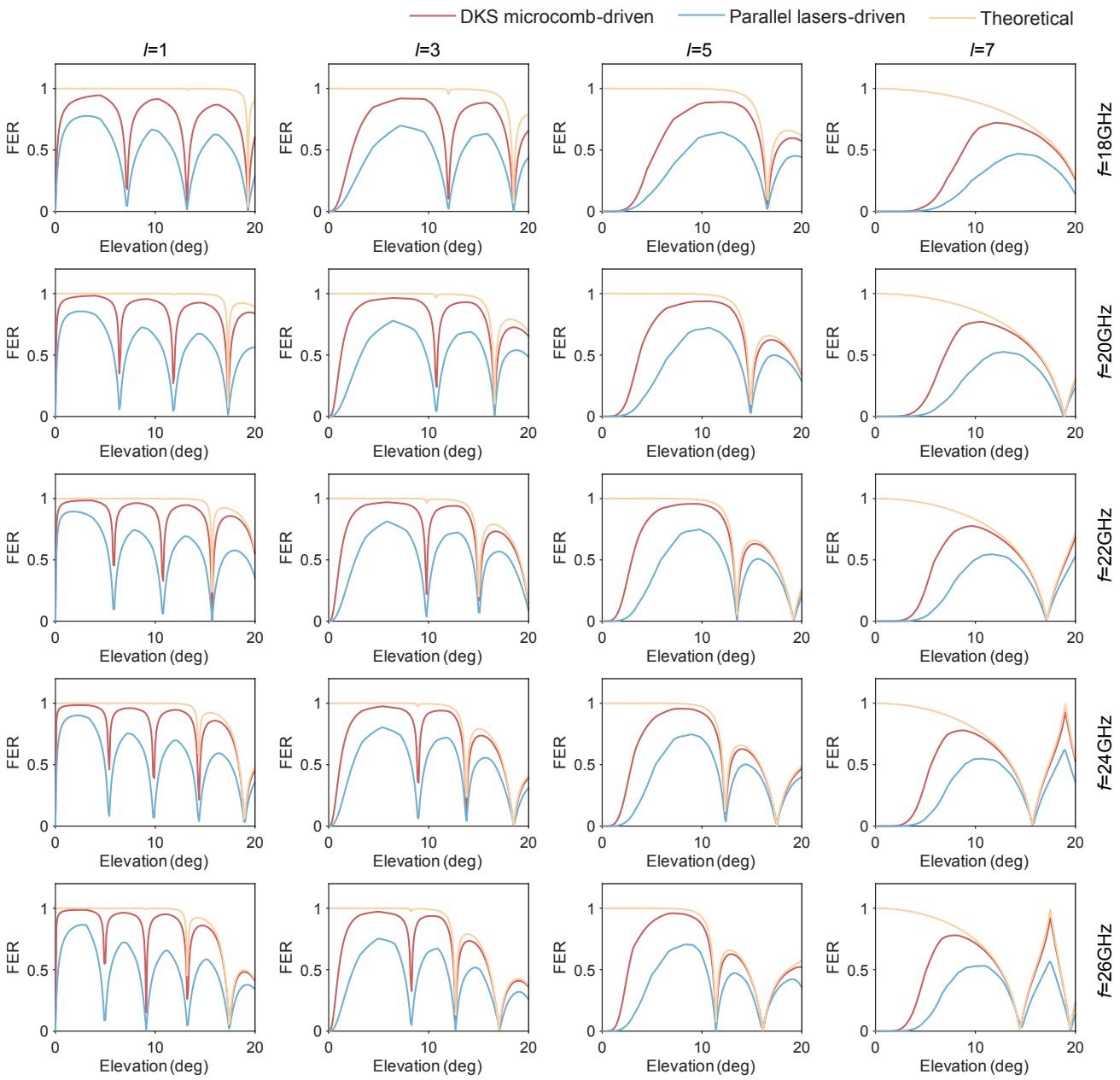

Figure S3. Measured FER across operation bandwidth and OAM modes.

yields an FER that closely approaches the theoretical limit across the entire 18-26 GHz frequency range. This robust consistency persists even at the frequency edges, where frequency-dependent phase dispersion and cabling imbalances typically degrade signal quality. In contrast, the parallel-laser system exhibits noticeable fluctuations and inferior mode purity relative to the theoretical baseline.

Furthermore, we evaluated the system's performance against the increasing complexity of wavefront synthesis by measuring FER across different OAM modes (l=1, 3, 5, 7), as shown in Figure. S3. Generating high-order OAM modes is inherently more sensitive to phase errors because the azimuthal phase gradient steepens ($2\pi l$) with the OAM mode number, acting as a magnifier for any source phase noise. The experimental results demonstrate that the microcomb-driven architecture sustains high purity levels comparable to the theoretical predictions, even for the challenging l=7 mode. Conversely, the parallel-laser baseline shows a deviation from the theoretical curve as the mode order increases, confirming that the ultra-narrow linewidth of the soliton comb lines and high-precision optical signal processing are critical for maintaining stable wavefront synthesis in high-performance sensing scenarios.

Supplementary Note 4: Vortex EM Sensing Model

The vortex EM transceiver employed in this work comprises a transmitting UCA and a single receiving antenna. To achieve high-resolution azimuth discrimination via OAM mode diversity [2, 3], the UCA is configured to synthesize multiple OAM modes through precise phase-coded feeding.

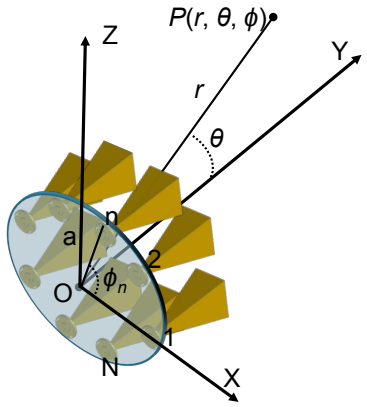

Figure S4. Model of vortex EM sensing.

As schematically illustrated in Figure. S4, the transmitting array consists of N antennas uniformly distributed on a circle of radius a. To generate a broadband vortex EM wave with OAM mode l, excitation signals with the same frequency but different initial phases are applied to each array element. Given that the azimuth angle of the n_{th} element is $\phi_n = 2\pi n/N$, the transmitted signal of the n_{th} element can be expressed as

$$s_n(t) = p_n(t) \exp\left(i2\pi f_c t + i\varphi_n\right) \tag{3}$$

where, f_c represents the carrier frequency, $p_n(t)$ is the complex envelope of the signal, and $\varphi_n = 2\pi ln/N$ is the initial phase of the n_{th} element. The maximum OAM mode that the array can generate follows the Nyquist criterion (i.e., $l_{max} < N/2$, where l_{max} is the maximum mode). For an arbitrary far-field point $U(r, \theta, \phi)$, the normalized electric field can be given by:

$$\begin{aligned} E(l, \mathbf{r}) &= \sum_{n=0}^{N-1} \frac{1}{|\mathbf{r} - \mathbf{r}_n|} \exp\left(ik\,|\mathbf{r} - \mathbf{r}_n| + i\varphi_n\right) \\ &\approx \frac{\exp(ikr)}{r} \sum_{n=0}^{N-1} \exp\left(-ik\hat{\mathbf{r}} \cdot \mathbf{r}_n + il\phi_n\right) \\ &\approx Ni^{-l} \frac{\exp(ikr)}{r} \exp(il\phi) J_l(ka \sin\theta) \end{aligned} \tag{4}$$

where k is the wavenumber and $J_l(.)$ is the l^{th}-order Bessel function of the first kind. $\mathbf{r}$ and $\mathbf{r_n}$ are the position vectors of point U and the n_{th} element, respectively

Assume the target consists of M ideal scatterers, where the backscattering coefficient of the m_{th} scattering point is σ_m and its coordinates are (r_m, θ_m, ϕ_m). To minimize range profile distortion, the receiving antenna is placed in close proximity to the transmitter center. When the array transmits a vortex EM wave with topological charge l and wavenumber k, the echoes received by the single antenna element is:

$$\begin{aligned} S_r(l, k) =& N \exp\left(\frac{-il\pi}{2}\right) \sum_{m=1}^{M} \frac{\sigma_m}{r_m r'_m} J_l\left(ka \sin\theta_m\right) \cdot \\ & \exp\left[ik\left(r_m + r'_m\right)\right] \exp\left(il\phi_m\right) \end{aligned} \tag{5}$$

where r'_m is the distance from the m_{th} scatterer to the receiver. As can be seen from the phase term in Eq. (5), the range information relates to wave number k, while azimuth information correlates with OAM mode l. This relationship enables target image reconstruction using two-dimensional Fourier transform. In the multiple-input single-output (MISO) configuration used here, the echo model contains a single Bessel factor. As discussed in the

Methods of the main text, this can introduce a mode-dependent sign reversal in the echo envelope. Therefore, a mode-wise phase compensation is applied before the two-dimensional Fourier reconstruction in order to remove this ambiguity and recover a single dominant azimuthal main lobe.

Supplementary Note 5: Vortex EM Sensing Error Analysis

The performance of vortex EM wave sensing critically depends on the purity of the radiated field distribution [4]. Ideally, vortex EM waves carrying integer OAM modes exhibit strictly linear phase variation with azimuth angle, termed pure-mode vortex EM waves. However, in practical hardware implementations, the existence of various errors degrades mode purity and alter radiation intensity distribution. Since the azimuthal discrimination of the present system relies on the phase structure of the generated vortex EM wave, non-ideal phase distributions degrade the focusing performance in the reconstructed image. In addition, low-quality radiation fields will destroy the orthogonality between different OAM modes, thereby affecting the performance of vortex EM waves in applications such as communication. To this end, we conduct an analysis of the factors affecting the quality of vortex EM radiation fields, laying a foundation for targeted improvement methods. Assuming that the amplitude error of the n_{th} array element is δA_n and the phase error is $\delta\varphi_n$, the actual excitation signal of the nth array element can be expressed as:

$$e_n = (A_n + \delta A_n)\, e^{i(l\phi_n + \delta\varphi_n)} \tag{6}$$

The resulting Array Factor (AF) for the UCA is derived as:

$$\begin{aligned} AF(\theta,\phi) &= \sum_{n=1}^{N} (A_n + \delta A_n) \frac{\exp\left(ik\left|\mathbf{r} - \mathbf{r}_n\right| + i\left(l\phi_n + \delta\varphi_n\right)\right)}{\left|\mathbf{r} - \mathbf{r}_n\right|} \\ &\approx \frac{\exp(ikr)}{r} \sum_{n=1}^{N} (A_n + \delta A_n) \exp\left(-i\left(k\hat{\mathbf{r}}\cdot\mathbf{r}_n - l\phi_n\right) + i\delta\varphi_n\right) \end{aligned} \tag{7}$$

Normally, the amplitudes of the excitation signals of each array element are the same. With normalized amplitudes, $A_n = 1$. Expanding the phase error term $e^{i\delta\varphi_n}$ via first-order Taylor approximation:

$$e^{i\delta\varphi_n} = 1 + i\delta\varphi_n + o\left(i\delta\varphi_n\right) \tag{8}$$

Substituting Eq. (8) into Eq. (7) yields:

$$\begin{aligned} AF(\theta,\phi) &\approx \frac{\exp(ikr)}{r} \sum_{n=1}^{N} (1 + \delta A_n) \exp\left(-i\left(k\hat{\mathbf{r}}\cdot\mathbf{r}_n - l\phi_n\right)\right) \cdot (1 + i\delta\varphi_n) \\ &= \frac{\exp(ikr)}{r} \sum_{n=1}^{N} (1 + \delta A_n + i\delta\varphi_n + \delta A_n i\delta\varphi_n) \exp\left(-i\left(k\hat{\mathbf{r}}\cdot\mathbf{r}_n - l\phi_n\right)\right) \\ &= N i^{-l} \frac{\exp(ikr)}{r} J_l(ka\sin\theta) \exp\left(il\phi_n\right) \\ &+ \frac{\exp(ikr)}{r} \sum_{n=1}^{N} \delta A_n \exp\left(-ika\sin\theta\cos\left(\phi - \phi_n\right)\right) \exp\left(il\phi_n\right) \\ &+ \frac{i\exp(ikr)}{r} \sum_{n=1}^{N} \delta\varphi_n \exp\left(-ika\sin\theta\cos\left(\phi - \phi_n\right)\right) \exp\left(il\phi_n\right) \\ &+ \frac{i\exp(ikr)}{r} \sum_{n=1}^{N} \delta A_n\delta\varphi_n \exp\left(-ika\sin\theta\cos\left(\phi - \phi_n\right)\right) \exp\left(il\phi_n\right) \end{aligned} \tag{9}$$

It can be seen from Eq. (9) that the array factor of the UCA with amplitude-phase errors comprises four components. The first term represents the error-free response. The dominant degradation stems from the second and third terms, representing contributions from amplitude and phase errors, respectively. The fourth term represents higher-order cross-coupling effects arising from amplitude-phase error interactions. In the present work, the total error budget can be interpreted as the combination of intra-channel distortions and inter-channel mismatches. The intra-channel terms represent frequency-dependent amplitude and phase variations within each channel, whereas the inter-channel terms describe channel-to-channel mismatch and relative phase nonuniformity. It is assumed that

the amplitude error and phase error of each array element satisfy the uniform distribution:

$$\begin{aligned} \delta A_n &\sim U\left(-\Lambda_e, \Lambda_e\right) \\ \delta \varphi_n &\sim U\left(-\Phi_e, \Phi_e\right) \end{aligned} \tag{10}$$

where Λ_e and Φ_e denote the maximum error bounds for amplitude and phase, respectively. The total error budget is a superposition of intra-channel fluctuations and inter-channel mismatches:

$$\begin{aligned} \Lambda_e &= \delta A_{\text{intra}} + \delta A_{\text{inter}} \\ \Phi_e &= \delta \varphi_{\text{intra}} + \delta \varphi_{\text{inter}} \end{aligned} \tag{11}$$

This analysis explains why both broadband flatness within each channel and stable synchronization among channels are important for preserving the quality of vortex EM fields. In the context of the present comparison, reduced inter-channel phase drift and more stable channel-to-channel coherence are consistent with the higher field purity observed for the microcomb-driven system.

References

[1] Yuan, T., Cheng, Y., Wang, H. & Qin, Y., Mode characteristics of vortical radio wave generated by circular phased array: theoretical and experimental results, *IEEE Trans. Antennas Propag.* **65**, 688–695 (2017).

[2] Cheng, M., Jiang, W., Guo, L., Li, J. & Forbes, A., Metrology with a twist: probing and sensing with vortex light, *Light Sci. Appl.* **14**, 4 (2025).

[3] Liu, K., Cheng, Y., Gao, Y., Li, X., Qin, Y. & Wang, H., Super-resolution radar imaging based on experimental OAM beams, *Appl. Phys. Lett.* **110**, 164102 (2017).

[4] Huang, Y., Li, X., Li, Q. et al., Generation of broadband high-purity dual-mode OAM beams using a four-feed patch antenna: theory and implementation, *Scientific Reports* **9**, 49377 (2019).